 CMES, vol.38, no.3, pp.231-261, 2008

Analysis of rectangular square plates by the mixed Meshless Local Petrov-Galerkin (MLPG) approach

T. Jarak[1] **and J. Sorić**[1]

Abstract: A new mixed meshless formulation based on the interpolation of both strains and displacements has been proposed for the analysis of plate deformation responses. Kinematics of a three dimensional solid is adopted and discretization is performed by the nodes located on the upper and lower plate surfaces. The governing equations are derived by employing the local Petrov-Galerkin approach. The approximation of all unknown field variables is carried out by using the same Moving Least Squares functions in the in-plane directions, while linear polynomials are applied in the transversal direction. The shear locking effect is efficiently minimized by interpolating the strain field independently from the displacements. The Poisson's thickness locking phenomenon is eliminated by introducing a new procedure based on the modification of the nodal values for the normal transversal strain component. The numerical efficiency of the derived algorithm is demonstrated by the numerical examples.

Keywords: mixed approach, plates, MLPG, shear locking, thickness locking

1 Introduction

In recent years, a new class of numerical approaches commonly known as meshless methods has attracted a considerable attention due to its potential to overcome some difficulties associated with the mesh-based numerical methods, such as the Finite Element Method (FEM). Using these new numerical procedures, a computational model may be discretized only by a set of the nodes which do not need to be connected into elements. Therefore, some issues associated with FEM, such as time-consuming mesh generation or element distortion problems, may be resolved by using meshless formulations.

Furthermore, it has been found out that meshless methods can also successfully deal with various locking phenomena in the thin-walled structure analysis. There-

[1] Faculty of Mechanical Engineering and Naval Architecture, University of Zagreb, Ivana Lučića 5, 10000 Zagreb, Croatia.

fore, a number of different meshless formulations were proposed. However, some of these approaches still require certain meshes. For example, in the Element-Free Galerkin (EFG) method [Krysl and Belytschko (1995, 1996); Noguchi, Kawashima and Miyamura (2000)], background cells are needed to integrate weak forms, while in the formulations based on a nodal integration [Wang and Chen (2004); Chen and Wang (2006)], a solution domain has to be discretized by employing the Delaunay triangulation. In contrast, the Meshless Local Petrov-Galerkin (MLPG) method [Atluri (2004)] does not require any kind of element mesh or background cells for either interpolation or integration and therefore represents a truly meshless approach. So far, the MLPG mathod has been successfully applied for solving various problems involving thin-walled structures, such as elasto-statics of homogenous plates [Long and Atluri (2002), Sorić, Li, Jarak and Atluri (2004); Sladek, Sladek, Mang (2002)], the analysis of composite plates [Gilhooley, Batra, Xiao, McCarthy and Gillespie (2007)] or elasto-dynamics of plate structures [Sladek, Sladek and Mang (2003), Qian, Batra and Chen (2004)]. Recently, the MLPG formulations for the analysis of shear-deformable shells [Sladek, Sladek, Wen and Aliabadi (2006); Sladek, Sladek, Krivacek and Aliabadi (2007)] as well as a 3-D continuum based MLPG shell algorithm [Jarak, Sorić and Hoster (2007)], have been developed.

However, most of the mentioned meshless formulations are based on some of the classical shell theories, e.g. Kirchhoff-Love theory [Krysl and Belytschko (1995, 1996); Long and Atluri (2002)] or Reissner-Mindlin theory [Donning and Liu (1998); Noguchi, Kawashima and Miyamura (2000); Chen and Wang (2006); Sladek, Sladek, Wen and Aliabadi (2006)]. The common drawback of such approaches is that they don't allow the implementation of a general three-dimensional (3-D) material law, which may be important in the modeling of shell-like structural components, especially in case of material nonlinearities. On the other hand, algorithms based on the higher order shell theories [Qian, Batra and Chen (2003); Qian, Batra and Chen (2004); Ferreira, Roque and Jorge (2006); Gilhooley, Batra, Xiao, McCarthy and Gillespie (2007)] are time-consuming and demand a large computation effort. Similary, in the direct 3-D meshless continuum formulation presented in [Li, Hao and Liu (2000)], at least three node layers in the structure thickness direction are necessary to successfully analyze shell structures, which considerably decreases the numerical efficiency. In addition, various locking effects still present serious obstacles in meshless methods, especially if derived formulations are based only on the approximation of the displacement field. Therefore, a more efficient meshless approach for the modeling of shell-like structures is desirable.

In the present contribution a new MLPG formulation, which is based on the mixed approach proposed in [Atluri, Han and Rajendran (2004)], is developed for the plate analysis. This new strategy has so far been applied to solve the 4^{th} order ordinary

differential equations [Atluri and Shen (2005), as well as complicated nonlinear dynamic problems [Han, Rajendran and Atluri (2005)]. The discretized system of equations is derived by independently approximating both the strain and displacement field. The formulation presented in this work is based on the concept of a 3-D solid, allowing the implementation of complete 3-D material models. The discretization of the plate continuum is carried out by the couples of nodes, where the nodes are located on the upper and lower plate surfaces. According to the MLPG method, for each node couple a Local Weak Form (LWF) of the standard 3-D equilibrium equations is written in terms of the strain components over a small area surrounding the node couple, which is called a local sub-domain. Thereby, the test functions that are linear through the plate thickness are employed. Since LWF contains more nodal unknowns than available equations, the standard 3-D strain-displacement relations are enforced only at the nodes in order to eliminate the nodal strain values from the equations. In this way, the closed global system of equations is obtained with only the nodal displacements as the unknown variables. Analogous to the solid-shell finite element formulations, such as those presented in [Tan and Vu-Quoc (2005); Klinkel, Gruttmann and Wagner (2006)] and the references therein, the approximation of the field variables are performed separately in the transversal and in the in-plane directions. Simple polynomials are utilized in the transversal direction, while the Moving Least Squares (MLS) approximation scheme is employed in the in-plane directions. Since the MLS functions don't posses the Kronecker delta property, the essential boundary conditions are enforced by using the penalty method.

It is known from the FEM literature that the solid-shell finite elements based only on the approximation of displacements are plagued by Poisson's thickness locking if the transversal displacement component is linear through the structure thickness. In that case, the normal transversal strain component computed directly from displacements does not vary through the thickness and locking arises if the Poisson's coefficient is different from zero. In the framework of meshless methods, this thickness locking effect has been eliminated by applying the hierarchical quadratic displacement interpolation through the thickness for the transversal displacement component in [Sorić, Li, Jarak and Atluri (2004); Jarak, Sorić and Hoster (2007)]. Although such procedure is efficient, the additional unknowns appear due to the quadratic interpolation, which have to be eliminated by employing the costly static condensation. On the other hand, the formulations based on the higher order shell theories, such as [Qian, Batra and Chen (2003)] are not plagued by the Poisson's thickness locking effect, but they are computationally and time-consuming. In the proposed mixed formulation, the Poisson's thickness locking phenomenon is avoided by applying a new procedure, where the linear distribution through the

thickness for the normal transversal strain component is enforced by modifying the kinematically compatible nodal strain values.

Furthermore, the meshless methods based only on the approximation of the displacement field generally exhibit the severe locking effects in the thin plate limit, especially if the approximation functions of the low order are used. In [Krysl and Belytschko (1996)] the membrane locking effect has been alleviated by employing the approximation functions of a sufficiently high order. The similar technique is used for dealing with the shear locking phenomenon in the formulations presented in [Garcia, Fancello de Barcellos and Duarte (1998); Noguchi, Kawashima, Miyamura (2000), Liu, Chua and Ghista (2006); Jarak, Sorić and Hoster (2007)]. In [Donning and Liu (1998); Kanok-Nukulchai, Barry, Saran-Yasoontorn and Bouillard (2001)] it has been proposed to construct the rotation field shape functions by the differentiation of the displacement field so as to eliminate the field incompatibility. However, it has been proved in [Tiago and Leitão (2007)] that such approach may yield a singular global system of equations within the Galerkin method because the approximation functions for the rotation field are linearly dependent. In contrast to those approaches, in the EFG formulations based on the stabilized nodal conforming integration [Wang and Chen (2004); Chen and Wang (2006)], a mixed concept has been adopted. Although such approach is numerically efficient due to the nature of the nodal integration, the employed approximation functions have to satisfy special requirements such as the Kirchhoff mode reproducing conditions under pure bending and the integration constraints needed for achieving the bending exactness. Consequently, the curvature smoothing stabilization procedure for the integration of the bending energy has to be applied in order to eliminate shear locking.

In the MLPG framework, a mixed approach for the analysis of plate structures has been proposed in [Li, Sorić, Jarak and Atluri (2005)], where shear locking is alleviated by properly choosing the field variables, which include the transversal shear strains and some of the displacement components. In the present work, the shear locking effect is eliminated simply by approximating the strain components independently from the displacement field. Thereby, the same low-order MLS functions are used for the interpolation of both the strains and displacements without setting any additional constraints on the trial functions.

The proposed mixed algorithm is computationally superior to the MLPG approach based only on the approximation of displacements, usually called the primal MLPG method [Atluri, Han and Rajendran (2004)]. In contrast to the primal meshless formulations, the shear locking effect in the thin plate limit may be efficiently alleviated without increasing the order of the MLS approximation functions. Consequently, the lower order of the MLS functions enables the use of smaller support

domains, and fewer quadrature points are needed for the numerical integration of LWF than in the primal MLPG formulation. Numerical efficiency and stability are further increased because the differentiation of the MLS functions over the local sub-domains is avoided, since their derivatives are needed only at the nodes. Finally, the accuracy and numerical efficiency of the proposed mixed meshless approach are demonstrated by the numerical examples.

2 MLPG mixed approach for plate analysis

In order to derive the governing equations for the proposed formulation, a homogeneous plate of uniform thickness is considered. The 3-D Cartesian co-ordinate system with the X^1-X^2 plane lying on the plate middle surface is used, as shown in Fig. 1.

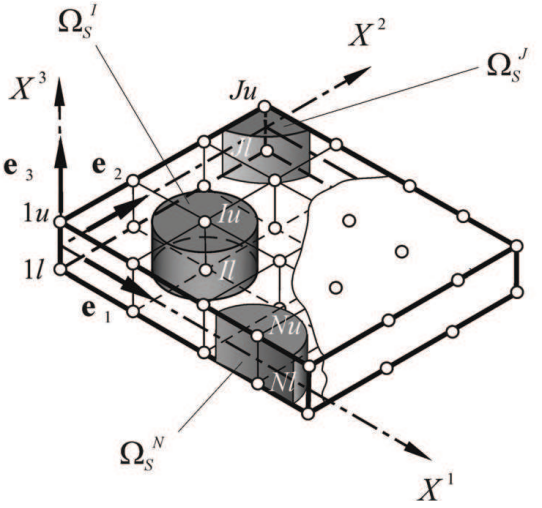

Figure 1: Discretization of plate continuum

The well known equilibrium equations referring to such coordinate system may be written for a global 3-D plate domain Ω bounded by a global surface Γ as

$$\sigma_{ij,j} + b_i = 0, \text{ in } \Omega, \tag{1}$$

where σ_{ij} is the stress tensor and b_i denotes the body force vector. On the surface Γ the following boundary conditions are given

$$u_i = \bar{u}_i, \text{ on } \Gamma_u, \tag{2}$$

$$t_i = \sigma_{ij} n_j = \bar{t}_i, \text{ on } \Gamma_t. \tag{3}$$

Herein, Γ_u and Γ_t are the parts of the global boundary Γ with the prescribed displacements $\bar{u}_i$ and tractions $\bar{t}_i$, respectively. n_j denotes direction cosines of the outward normal vector on Γ.

The plate continuum is discretized by a set of node couples, where the nodes are positioned on the upper and lower plate surface as shown in Fig. 1. According to the Local Petrov-Galerkin approach [Atluri 2004], the equilibrium equations (1) may be written in a weak form over the local sub-domain Ω_s^I, which surrounds the I^{th} node couple and is bounded by the local boundary surface $\partial\Omega_s^I$, as

$$\int_{\Omega_s^I} v_{ik}\left(\sigma_{kj,j}+b_k\right)\,\mathrm{d}\Omega-\alpha\int_{\Gamma_{su}^I} v_{ik}(u_k^{(h)}-\bar{u}_k)\,\mathrm{d}\Gamma=0;\quad I=1,2,...,N, \tag{4}$$

where N stands for the total number of node couples used for the plate discretization. $u_k^{(h)}$ denotes the trial function describing the displacement field, and v_{ik} represents the applied test functions. Since the trial functions used in this work don't posses the interpolation property at the nodes, the essential boundary conditions are imposed by employing the penalty method with $\alpha >> 1$ as a penalty parameter. Γ_{su}^I is the part of $\partial\Omega_s^I$ with the prescribed displacements $\bar{u}_k$. It is to note that Ω_s^I could theoretically be of any geometric shape and size. Furthermore, according to the Petrov-Galerkin principle, the test and trial functions may be taken from different functional spaces. According to [Atluri and Zhu 2000], the test functions are chosen such that $v_{ik}=\delta_{ik}v$, where v is a kinematically admissible test function and δ_{ik} denotes the Kronecker delta. In the present contribution, cylindrical local sub-domains as shown in Fig. 1 are used and v is assumed to be linear over the plate thickness

$$v\left(X^j\right)=c_0+c_1X^3, \tag{5}$$

with c_0 and c_1 as arbitrary real constants.

By inserting Eq. (5) in Eq. (4), using the divergence theorem and taking $t_i=n_j\sigma_{ij}$ on $\partial\Omega_s^I$ into account, LWF may be rewritten in the following form

$$-\int_{\partial\Omega_s^I} t_i\mathrm{d}\Gamma-\int_{\Omega_s^I} b_i\,\mathrm{d}\Omega+\alpha\int_{\Gamma_{su}^I}\left(u_i^{(h)}-\bar{u}_i\right)\mathrm{d}\Gamma=0, \tag{6}$$

$$\int_{\partial\Omega_s^I}\left(X^3\right)_{,j}\sigma_{ij}\,\mathrm{d}\Omega-\int_{\Gamma_s^I}X^3t_i\mathrm{d}\Gamma-\int_{\Omega_s^I}X^3\,b_i\,\mathrm{d}\Omega+\alpha\int_{\Gamma_{su}^I}X^3\left(u_i^{(h)}-\bar{u}_i\right)\mathrm{d}\Gamma=0,\ I=1,2,...,N. \tag{7}$$

Herein, Eqs. (6) and (7) relate to the constant and linear term of the test function (5), respectively. More details can be found in [Sorić, Li, Jarak and Atluri (2004)].

The stress tensor σ_{ij} and the tractions t_i may be obtained by employing the standard 3-D constitutive relations

$$\sigma_{ij} = C_{ijkl}\,\varepsilon_{kl} \tag{8}$$

with C_{ijkl} as the material tensor for the linear elastic isotropic homogeneous materials defined in the global Cartesian coordinates as

$$C_{ijkl} = \lambda\,\delta_{ij}\,\delta_{kl} + \mu\left(\delta_{ik}\,\delta_{jl} + \delta_{il}\,\delta_{jk}\right), \tag{9}$$

where $\lambda = \frac{E\,\nu}{(1+\nu)(1-2\,\nu)}$ and $\mu = \frac{E}{2(1+\nu)}$ are Lame's elastic constants.

After applying the constitutive relations (8) and imposing the natural boundary conditions (3) on the local boundary $\partial\Omega_s^I$, the following form of LWF is obtained

$$-\int_{L_S^I} C_{ijkl}\,\varepsilon_{kl}^{(h)}\,n_j\mathrm{d}\Gamma - \int_{\Gamma_{Su}^I} C_{ijkl}\,\varepsilon_{kl}^{(h)}\,n_j\mathrm{d}\Gamma + \alpha\int_{\Gamma_{su}^I} u_i^{(h)}\,\mathrm{d}\Gamma = \int_{L_{St}^I} \bar{t}_i\mathrm{d}\Gamma + \int_{\Omega_s^I} b_i\,\mathrm{d}\Omega + \alpha\int_{\Gamma_{su}^I} \bar{u}_i\,\mathrm{d}\Gamma, \tag{10}$$

$$\int_{\Omega_s^I} \left(X^3\right)_{,j} C_{ijkl}\,\varepsilon_{kl}^{(h)}\mathrm{d}\Omega - \int_{L_S^I} X^3\,C_{ijkl}\,\varepsilon_{kl}^{(h)}\,n_j\mathrm{d}\Gamma - \int_{\Gamma_{Su}^I} X^3\,C_{ijkl}\,\varepsilon_{kl}^{(h)}\,n_j\mathrm{d}\Gamma + \alpha\int_{\Gamma_{su}^I} X^3\,u_i^{(h)}\,\mathrm{d}\Gamma = \int_{L_{St}^I} X^3\,\bar{t}_i\mathrm{d}\Gamma + \int_{\Omega_s^I} X^3\,b_i\,\mathrm{d}\Omega + \alpha\int_{\Gamma_{su}^I} X^3\,\bar{u}_i\,\mathrm{d}\Gamma, \quad I = 1,2,...,N, \tag{11}$$

where both the strains $\varepsilon_{kl}^{(h)}$ and the displacements $u_i^{(h)}$ are considered as independent variables. The local boundary $\partial\Omega_s^I$ is divided into three parts, $\partial\Omega_s^I = L_s^I \cup \Gamma_{st}^I \cup \Gamma_{su}^I$, where L_s^I is the part of $\partial\Omega_s^I$ inside the global domain Γ, while Γ_{st}^I and Γ_{su}^I coincide with the parts of Γ with the prescribed natural and essential boundary conditions, respectively.

Linear distribution over the plate thickness is assumed for all displacement and strain components, which may be written as

$$u_i^{(h)}\left(X^k\right) = \alpha\left(X^3\right)u_{i(u)}^{(h)}\left(X^\alpha\right) + \beta\left(X^3\right)u_{i(l)}^{(h)}\left(X^\alpha\right), \tag{12}$$

$$\varepsilon_{ij}^{(h)}\left(X^k\right)=\alpha\left(X^3\right)\varepsilon_{ij(u)}^{(h)}\left(X^\alpha\right)+\beta\left(X^3\right)\varepsilon_{ij(l)}^{(h)}\left(X^\alpha\right), \tag{13}$$

$$\alpha\left(X^3\right)=\frac{1}{2}+\frac{X^3}{h},\ \beta\left(X^3\right)=\frac{1}{2}-\frac{X^3}{h}. \tag{14}$$

In the above equations, $\alpha\left(X^3\right)$ and $\beta\left(X^3\right)$ describe a linear distribution of the strain and displacement components, while $\varepsilon_{ij(u)}^{(h)}\left(X^\alpha\right)$, $\varepsilon_{ij(l)}^{(h)}\left(X^\alpha\right)$ and $u_{i(u)}^{(h)}\left(X^\alpha\right)$, $u_{i(l)}^{(h)}\left(X^\alpha\right)$ denote the strains and displacements on the upper and lower plate surface, respectively. h stands for the plate thickness.

It is to note that Eqs. (10) and (11) represent a system of 6 equations for each local sub-domain Ω_s^I, while in Eqs. (12) and (13) there are altogether 18 unknown variables, including the 6 strain and 3 displacement components on the upper and lower surfaces. Therefore, in order to derive a closed system of equations on the structural level, the following kinematics constraints are imposed for each Ω_s^I

$$\int_{\Omega_S^I} v_{(ij)}^{(\varepsilon)}\left[\varepsilon_{ij}^{(h)}\left(X^k\right)-\varepsilon_{ij}\left(X^k\right)\right]\mathrm{d}\Omega=0,\ I=1,2,...,N, \tag{15}$$

where $\varepsilon_{ij}^{(h)}\left(X^k\right)$ denotes the assumed strains, while $\varepsilon_{ij}\left(X^k\right)$ stands for the strains calculated from the approximated displacements by means of the standard linear 3-D strain-displacement relations

$$\varepsilon_{ij}\left(X^k\right)=\frac{1}{2}\left(u_{i,j}^{(h)}\left(X^k\right)+u_{j,i}^{(h)}\left(X^k\right)\right). \tag{16}$$

For the purpose of generalization the kinematics constraints in Eq. (15) are written in the local weak form with $v_{(ij)}^{(\varepsilon)}$ as appropriate test functions. By conveniently choosing the test functions, the additional 12 equations, which are needed for closing the global system of equations, may be obtained for each Ω_s^I.

3 Discretization

Various numerical schemes for the approximation of the data for randomly scattered points are currently used in meshless methods [Liu (2003), Atluri (2004)], one of the most popular being the Moving Least Squares (MLS) method. In the present work, all displacement and strain components on the upper and lower plate surfaces are approximated in the in-plane directions by employing the same MLS shape functions, leading to

$$u_{i(u)}^{(h)}\left(X^\delta\right)=\sum_{J=1}^{n}\phi^J\left(X^\delta\right)\hat{u}_{i(u)}^J,\quad u_{i(l)}^{(h)}\left(X^\delta\right)=\sum_{J=1}^{n}\phi^J\left(X^\delta\right)\hat{u}_{i(l)}^J, \tag{17}$$

$$\varepsilon^{(h)}_{ij(u)}\left(X^{\delta}\right)=\sum_{J=1}^{n}\phi^{J}\left(X^{\delta}\right)\hat{\varepsilon}^{J}_{ij(u)},\quad \varepsilon^{(h)}_{ij(l)}\left(X^{\delta}\right)=\sum_{J=1}^{n}\phi^{J}\left(X^{\delta}\right)\hat{\varepsilon}^{J}_{ij(l)}. \tag{18}$$

Here, $\phi^{J}\left(X^{\delta}\right)$ is the in-plane MLS shape function associated with the J^{th} node couple inside the domain of definition of the current point X^{δ}. Thereby, the domain of definition is a region that includes all nodes whose nodal MLS shape functions do not vanish at the current point, as defined in [Atluri and Zhu (1998)]. n stands for the total number of node couples inside the domain of definition.

The well-known MLS nodal shape function $\phi^{J}\left(X^{\delta}\right)$ is defined as

$$\phi^{J}\left(X^{\delta}\right)=\sum_{i=1}^{m}p_{i}(\bar{X}^{\delta})\left[\mathbf{A}^{-1}\mathbf{B}\right]_{iJ} \tag{19}$$

with $\mathbf{A}$ as a momentum matrix

$$\mathbf{A}=\sum_{J=1}^{n}W_{J}(X^{\delta})\mathbf{p}(\bar{X}^{\delta}_{J})\mathbf{p}^{T}(\bar{X}^{\delta}_{J}), \tag{20}$$

and the matrix $\mathbf{B}$ defined as

$$\mathbf{B}=\left[W_{1}(X^{\delta})\,\mathbf{p}(\bar{X}^{\delta}_{1})\quad W_{2}(X^{\delta})\,\mathbf{p}(\bar{X}^{\delta}_{2})\quad\cdots\quad W_{J}(X^{\delta})\,\mathbf{p}(\bar{X}^{\delta}_{J})\quad\cdots\quad W_{n}(X^{\delta})\,\mathbf{p}(\bar{X}^{\delta}_{n})\right]. \tag{21}$$

The complete monomial basis $\mathbf{p}\left(\bar{X}^{\delta}\right)$ is expressed in terms of the local normalized coordinates $\bar{X}^{\delta}$ in order to improve the conditioning of the matrix $\mathbf{A}$, as explained in [Jarak, Sorić and Hoster (2007)]. $W_{J}(X^{\delta})$ is a weight function associated with the J^{th} node couple, which is chosen as the 4^{th} order spline function

$$W_{J}(X^{\delta})=\begin{cases}1-6\left(\frac{d_{J}}{r_{J}}\right)^{2}+8\left(\frac{d_{J}}{r_{J}}\right)^{3}-3\left(\frac{d_{J}}{r_{J}}\right)^{4}; & 0\le d_{J}\le r_{J}\\ 0; & d_{J}>r_{J}\end{cases}, \tag{22}$$

where $d_{J}=\left|X^{\delta}-X^{\delta}_{J}\right|$ is the in-plane distance between the node couple J and the current sample point. The detailed mathematical description of the MLS approximation strategies can be found in [Fasshauer (2007)], and the references therein.

Eqs. (12) and (13) for the displacement and strain fields may be written in the discretized forms as

$$\mathbf{u}^{(h)}=\sum_{J=1}^{n}\mathbf{\Phi}^{J}_{u}\hat{\mathbf{u}}^{J}, \tag{23}$$

$$\boldsymbol{\varepsilon}^{(h)}=\sum_{J=1}^{n}\mathbf{\Phi}^{J}_{\varepsilon}\hat{\boldsymbol{\varepsilon}}^{J}. \tag{24}$$

Matrices $\mathbf{\Phi}_u^J$ and $\mathbf{\Phi}_\varepsilon^J$ contain the 3-D displacement and strain nodal shape functions defined as

$$\mathbf{\Phi}_u^J = \phi^J \left[\alpha \mathbf{I}_3 \quad \beta \mathbf{I}_3\right], \tag{25}$$

$$\mathbf{\Phi}_\varepsilon^J = \phi^J \left[\alpha \mathbf{I}_6 \quad \beta \mathbf{I}_6\right]. \tag{26}$$

In the above relations $\phi^J = \phi^J\left(X^1, X^2\right)$ represents the in-plane MLS approximation defined in Eq. (19), $\alpha = \alpha\left(X^3\right)$ and $\beta = \beta\left(X^3\right)$ describe the linear interpolation over the thickness, while $\mathbf{I}_3$ and $\mathbf{I}_6$ stand for the 3x3 and 6x6 identity matrices, respectively. $\hat{\mathbf{u}}^J$ and $\hat{\boldsymbol{\varepsilon}}^J$ are the vectors containing the unknown fictitious nodal displacement and strain values

$$\left(\hat{\mathbf{u}}^J\right)^T = \left[\left(\hat{\mathbf{u}}_{(u)}^J\right)^T \quad \left(\hat{\mathbf{u}}_{(l)}^J\right)^T\right], \ \left(\hat{\boldsymbol{\varepsilon}}^J\right)^T = \left[\left(\hat{\boldsymbol{\varepsilon}}_{(u)}^J\right)^T \quad \left(\hat{\boldsymbol{\varepsilon}}_{(l)}^J\right)^T\right]. \tag{27}$$

Herein, $\hat{\mathbf{u}}_{(u)}^J$ and $\hat{\mathbf{u}}_{(l)}^J$ are the vectors of the nodal displacements associated with the upper and lower nodes

$$\left(\hat{\mathbf{u}}_{(u)}^J\right)^T = \left[\hat{u}_{1(u)}^J \quad \hat{u}_{2(u)}^J \quad \hat{u}_{3(u)}^J\right], \ \left(\hat{\mathbf{u}}_{(l)}^J\right)^T = \left[\hat{u}_{1(l)}^J \quad \hat{u}_{2(l)}^J \quad \hat{u}_{3(l)}^J\right], \tag{28}$$

and $\hat{\boldsymbol{\varepsilon}}_{(u)}^J$ and $\hat{\boldsymbol{\varepsilon}}_{(l)}^J$ denote the corresponding nodal strain vectors

$$\begin{aligned}
\left(\hat{\boldsymbol{\varepsilon}}_{(u)}^J\right)^T &= \left[\hat{\varepsilon}_{11(u)}^J \quad \hat{\varepsilon}_{22(u)}^J \quad \hat{\varepsilon}_{33(u)}^J \quad \hat{\gamma}_{12(u)}^J \quad \hat{\gamma}_{23(u)}^J \quad \hat{\gamma}_{13(u)}^J\right], \\
\left(\hat{\boldsymbol{\varepsilon}}_{(l)}^J\right)^T &= \left[\hat{\varepsilon}_{11(l)}^J \quad \hat{\varepsilon}_{22(l)}^J \quad \hat{\varepsilon}_{33(l)}^J \quad \hat{\gamma}_{12(l)}^J \quad \hat{\gamma}_{23(l)}^J \quad \hat{\gamma}_{13(l)}^J\right].
\end{aligned} \tag{29}$$

Employing the strain field approximation (24) and the constitutive relations (8) and (9), the stress and traction may be calculated in terms of the nodal strains as

$$\boldsymbol{\sigma} = \mathbf{D} \sum_{J=1}^{n} \mathbf{\Phi}_\varepsilon^J \hat{\boldsymbol{\varepsilon}}^J, \tag{30}$$

$$\mathbf{t} = \mathbf{N}\mathbf{D} \sum_{J=1}^{n} \mathbf{\Phi}_\varepsilon^J \hat{\boldsymbol{\varepsilon}}^J, \tag{31}$$

where $\mathbf{D}$ is the 3-D elasticity stress-strain matrix and $\boldsymbol{\sigma}$ is the complete stress vector

$$\boldsymbol{\sigma}^T = \left[\sigma_{11} \quad \sigma_{22} \quad \sigma_{33} \quad \tau_{12} \quad \tau_{23} \quad \tau_{13}\right]. \tag{32}$$

In Eq. (31) $\mathbf{t} = t_i \mathbf{e}_i$ denotes the traction vector and the matrix $\mathbf{N}$ is defined as

$$\mathbf{N} = \begin{bmatrix} n_1 & 0 & 0 & n_2 & 0 & n_3 \\ 0 & n_2 & 0 & n_1 & n_3 & 0 \\ 0 & 0 & n_3 & 0 & n_2 & n_1 \end{bmatrix}, \tag{33}$$

where n_i denotes the components of the outward unit normal vector on $\partial\Omega_s^I$, $\mathbf{n} = n_i\,\mathbf{e}_i$.

By means of Eqs. (23)-(33), LWFs (10) and (11) are transformed into the following discretized system of linear equations on the domain of influence level related to the I^{th} node couple

$$\sum_{J=1}^{N_I}\left[-\int_{L_S^I}\mathbf{N}\mathbf{D}\boldsymbol{\Phi}_\varepsilon^J\mathrm{d}\Gamma-\int_{\Gamma_{Su}^I}\mathbf{N}\mathbf{D}\boldsymbol{\Phi}_\varepsilon^J\mathrm{d}\Gamma\right]\hat{\boldsymbol{\varepsilon}}^J+\alpha\sum_{J=1}^{N_I}\left[\int_{\Gamma_{su}^I}\boldsymbol{\Phi}_u^J\mathrm{d}\Gamma\right]\hat{\mathbf{u}}^J$$
$$=\int_{\Gamma_{St}^I}\bar{\mathbf{t}}\,\mathrm{d}\Gamma+\int_{\Omega_s^I}\mathbf{b}\,\mathrm{d}\Omega+\alpha\int_{\Gamma_{su}^I}\bar{\mathbf{u}}\,\mathrm{d}\Gamma, \quad (34)$$

$$\sum_{J=1}^{N_I}\left[\int_{\Omega_s^I}\mathrm{grad}(\mathbf{v}_1)\mathbf{D}\boldsymbol{\Phi}_\varepsilon^J\mathrm{d}\Omega-\int_{L_S^I}X^3\mathbf{N}\mathbf{D}\boldsymbol{\Phi}_\varepsilon^J\,\mathrm{d}\Gamma-\int_{\Gamma_{Su}^I}X^3\mathbf{N}\mathbf{D}\boldsymbol{\Phi}_\varepsilon^J\mathrm{d}\Gamma\right]\hat{\boldsymbol{\varepsilon}}^J$$
$$+\alpha\sum_{J=1}^{N_I}\left[\int_{\Gamma_{su}^I}X^3\,\boldsymbol{\Phi}_u^J\mathrm{d}\Gamma\right]\hat{\mathbf{u}}^J=\int_{\Gamma_{St}^I}X^3\,\mathbf{t}\,\mathrm{d}\Gamma+\int_{\Omega_s^I}X^3\,\mathbf{b}\,\mathrm{d}\Omega+\alpha\int_{\Gamma_{su}^I}X^3\,\bar{\mathbf{u}}\,\mathrm{d}\Gamma,$$
$$I=1,2,...,N. \quad (35)$$

Thereby the domain of influence is a region that covers all nodes whose weight functions do not vanish in the local sub-domain surrounding the current node couple, as defined in [Atluri and Zhu (1998)]. In Eqs. (34) and (35), N_I denotes the total number of nodes inside the domain of influence of the I^{th} node couple and $\mathrm{grad}(\mathbf{v}_1)$ describes the gradient of the linear part of the test function (5)

$$\mathrm{grad}(\mathbf{v}_1)=\begin{bmatrix}X^3{}_{,1} & 0 & 0 & X^3{}_{,2} & 0 & X^3{}_{,3}\\ 0 & X^3{}_{,2} & 0 & X^3{}_{,1} & X^3{}_{,3} & 0\\ 0 & 0 & X^3{}_{,3} & 0 & X^3{}_{,2} & X^3{}_{,1}\end{bmatrix}=\begin{bmatrix}0&0&0&0&0&1\\0&0&0&0&1&0\\0&0&1&0&0&0\end{bmatrix}. \quad (36)$$

As already mentioned, in the discretized LWFs (34) and (35) more unknown variables appear then there are available equations. Therefore, the additional kinematics constraints (15) are employed by means of the collocation approach in order to reduce the overall number of unknowns.

By using the Dirac delta functions $\delta\left(\mathbf{X}-\mathbf{X}^{\mathbf{I}}_{(u)}\right)$ and $\delta\left(\mathbf{X}-\mathbf{X}^{\mathbf{I}}_{(l)}\right)$ as the test functions $v^{(\varepsilon)}_{(ij)}$ in Eq. (15), the kinematics relations (16) are imposed directly at the upper and lower nodes

$$\begin{aligned}
&\varepsilon^{(h)}_{ij}\left(\mathbf{X}^I_{(u)}\right)=\frac{1}{2}\left[u_{i,j}\left(\mathbf{X}^I_{(u)}\right)+u_{j,i}\left(\mathbf{X}^I_{(u)}\right)\right],\\
&\varepsilon^{(h)}_{ij}\left(\mathbf{X}^I_{(l)}\right)=\frac{1}{2}\left[u_{i,j}\left(\mathbf{X}^I_{(l)}\right)+u_{j,i}\left(\mathbf{X}^I_{(l)}\right)\right],\ I=1,2,...,N
\end{aligned} \tag{37}$$

with $\mathbf{X}^I_{(u)}=\left[X^1_I \quad X^2_I \quad X^3=0,5h\right]^T$ and $\mathbf{X}^I_{(l)}=\left[X^1_I \quad X^2_I \quad X^3=-0,5h\right]^T$ being the global Cartesian coordinates of the upper and lower node of the I^{th} node couple, respectively. The kinematic equations (37) are numerically implemented under the assumption that the nodal strain values are exactly interpolated, and it holds

$$\varepsilon^{(h)}_{ij}\left(\mathbf{X}^I_{(u)}\right)\approx\hat{\varepsilon}^I_{ij(u)},\quad \varepsilon^{(h)}_{ij}\left(\mathbf{X}^I_{(l)}\right)\approx\hat{\varepsilon}^I_{ij(l)},\quad I=1,2,...,N. \tag{38}$$

By applying the displacement interpolation (23) and the assumption (38) in Eq. (37), it is possible to express the nodal strain components in terms of the independently approximated displacements in a relatively simple and numerically efficient manner as

$$\hat{\boldsymbol{\varepsilon}}^I_{(u)}=\sum_{J=1}^{n_I}\mathbf{B}^{JI}_{(u)}\hat{\mathbf{u}}^J,\quad \hat{\boldsymbol{\varepsilon}}^I_{(l)}=\sum_{J=1}^{n_I}\mathbf{B}^{JI}_{(l)}\hat{\mathbf{u}}^J,\qquad I=1,2,...,N. \tag{39}$$

Herein, $\mathbf{B}^{JI}_{(u)}=\mathbf{B}^J\left(\mathbf{X}^I_{(u)}\right)$ and $\mathbf{B}^{JI}_{(l)}=\mathbf{B}^J\left(\mathbf{X}^I_{(l)}\right)$ stand for the 3D strain-displacement matrices calculated at the upper and lower node of the I^{th} node couple by the relation

$$\mathbf{B}^J=\begin{bmatrix}
\alpha\,\phi^J{}_{,1} & 0 & 0 & \beta\,\phi^J{}_{,1} & 0 & 0\\
0 & \alpha\,\phi^J{}_{,2} & 0 & 0 & \beta\,\phi^J{}_{,2} & 0\\
0 & 0 & \alpha_{,3}\,\phi^J & 0 & 0 & \beta_{,3}\,\phi^J\\
\alpha\,\phi^J{}_{,2} & \alpha\,\phi^J{}_{,1} & 0 & \beta\,\phi^J{}_{,2} & \beta\,\phi^J{}_{,1} & 0\\
0 & \alpha_{,3}\,\phi^J & \alpha\,\phi^J{}_{,2} & 0 & \beta_{,3}\,\phi^J & \beta\,\phi^J{}_{,2}\\
\alpha_{,3}\,\phi^J & 0 & \alpha\phi^J{}_{,1} & \beta_{,3}\,\phi^J & 0 & \beta\,\phi^J{}_{,1}
\end{bmatrix}. \tag{40}$$

Furthermore, in Eqs. (39) n_I is the total number of the nodes in the MLS domain of definition of the I^{th} node couple. As evident, by using the described collocation approach numerical integration in Eq. (15) is avoided, resulting in the reduction of computation time. If Eqs. (39) are inserted into the discretized LWFs (34) and (35), the closed system of linear algebraic equations with only the nodal displacements as unknowns may be obtained.

4 Poisson's thickness locking effect

It is well known that the undesired Poisson's thickness locking effect arises in the 3-D continuum based numerical formulations for plate and shell analyses if the normal transversal strain component ε_{33} does not vary through the structure thickness [Hauptmann and Schweizerhof (1998), Sze (2002)].

In our formulation the strain component ε_{33} is initially assumed to be linear through the thickness according to (13). Nevertheless, it can be shown that the linear distribution of the displacement component u_3 over the plate thickness leads to the appearance of the Poisson's thickness locking effect. Using Eqs. (39) and (40), it can be easily shown that

$$\hat{\varepsilon}^I_{33(u)} = \hat{\varepsilon}^I_{33(l)} = \frac{1}{h}\sum_{J=1}^{n_I} \phi^{JI}\hat{u}^K_{3(u)} - \frac{1}{h}\sum_{J=1}^{n_I} \phi^{JI}\hat{u}^J_{3(l)} \neq f\left(X^3\right),\ I = 1,2,...,N, \tag{41}$$

where $\phi^{JI} = \phi^J\left(X^1_I, X^2_I\right)$ are the in-plane MLS nodal shape functions calculated at the location of the I^{th} node couple. If these values for $\hat{\varepsilon}^I_{33(u)}$ and $\hat{\varepsilon}^I_{33(l)}$ are employed in Eq. (24) for the calculation of the strain field distribution, it is clear that the normal strain $\varepsilon^{(h)}_{33}$ is constant over the thickness, and the system locks if the Poisson's ratio is not equal to zero. Therefore, the condition $\hat{\varepsilon}^I_{33(u)} \neq \hat{\varepsilon}^I_{33(l)}$ has to be fulfilled in order to avoid the Poisson's thickness locking phenomenon.

For the elimination of this undesired locking effect, a new procedure based on the modification of the nodal strain component values $\hat{\varepsilon}^I_{33(u)}$ and $\hat{\varepsilon}^I_{33(l)}$ is proposed. For that purpose, the linear distribution over the thickness for ε_{33} may be written at the position of the node couples as

$$\varepsilon^{(h)}_{33}\left(X^1_I, X^2_I, X^3\right) = \left(\varepsilon^{(h)}_{33}\right)^{I0} + X^3\left(\varepsilon^{(h)}_{33,3}\right)^{I0},\ I = 1,2,...,N. \tag{42}$$

Here, $\left(\varepsilon^{(h)}_{33}\right)^{I0}$ and $\left(\varepsilon^{(h)}_{33,3}\right)^{I0}$ are the values of ε_{33} and its derivative with respect to X^3 calculated at the point $\mathbf{X}^I_{(0)}$, respectively. The point $\mathbf{X}^I_{(0)}$ is positioned on the plate middle surface between the nodes of the I^{th} node couple, as shown in Fig. 2. The constant term $\left(\varepsilon^{(h)}_{33}\right)^{I0}$ is computed directly from the approximated displacements by using Eq. (41), and the following statement holds,

$$\left(\varepsilon_{33}\right)^{I0} = \hat{\varepsilon}^I_{33(u)} = \hat{\varepsilon}^I_{33(l)} = u^{(h)}_{3,3}\left(\mathbf{X}^I_{(0)}\right). \tag{43}$$

By taking into account the assumption (38), the normal transversal nodal strains at

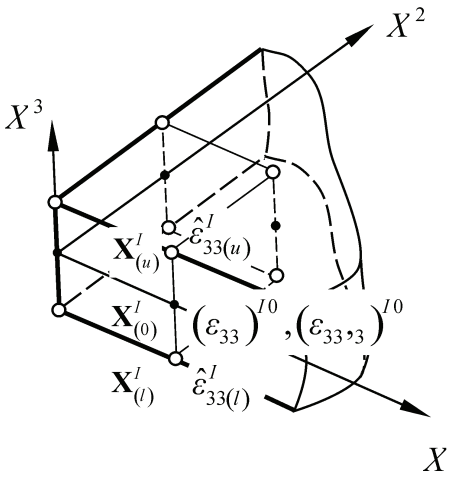

Figure 2: Discretization points with belonging variables used for the elimination of the Poisson's thickness locking effect

the upper and lower nodes may be written as

$$\begin{aligned}
&\hat{\tilde{\varepsilon}}^I_{33(u)} \approx \varepsilon^{(h)}_{33}\left(\mathbf{X}^I_{(u)}\right) = \hat{\varepsilon}^I_{33(u)} + \tfrac{h}{2}\left(\varepsilon^{(h)}_{33,3}\right)^{I0},\\
&\hat{\tilde{\varepsilon}}^I_{33(l)} \approx \varepsilon^{(h)}_{33}\left(\mathbf{X}^I_{(l)}\right) = \hat{\varepsilon}^I_{33(l)} - \tfrac{h}{2}\left(\varepsilon^{(h)}_{33.3}\right)^{I0},\\
&I = 1,2,...,N
\end{aligned} \tag{44}$$

with $\hat{\tilde{\varepsilon}}^I_{33(u)}$ and $\hat{\tilde{\varepsilon}}^I_{33(l)}$ as the new modified nodal values, which are not kinematically compatible with the displacement field. The derivative $\varepsilon^{(h)}_{33,3}$ is expressed by enforcing the additional equilibrium equation in the normal direction at the mid-point $\mathbf{X}^I_{(0)}$

$$\sigma_{3j,j}\left(\mathbf{X}^I_{(0)}\right) + b_3\left(\mathbf{X}^I_{(0)}\right) = 0,\ \ I = 1,2,...,N. \tag{45}$$

Accordingly, employing the constitutive equation for σ_{33} from Eq. (8), $\varepsilon^{(h)}_{33},_3$ may be calculated as

$$\begin{aligned}
&\left(\varepsilon^{(h)}_{33,3}\right)^{I0} = -\frac{1}{C_{3333}}\left(b_3 + C_{3311}\left(\varepsilon^{(h)}_{11,3}\right)^{I0}\right.\\
&\left. + C_{3322}\left(\varepsilon^{(h)}_{22,3}\right)^{I0} + C_{1313}2\left(\varepsilon^{(h)}_{13,1}\right)^{I0} + C_{2323}2\left(\varepsilon^{(h)}_{23,2}\right)^{I0}\right),\\
&\qquad\qquad\qquad\qquad\qquad\qquad\qquad\qquad I = 1,2,...,N,
\end{aligned} \tag{46}$$

where $(\,)^{I0}$ denotes the values at $\mathbf{X}^I_{(0)}$. By means of the strain approximation (24), the derivatives of the strain components on the right-hand side of Eq. (46) are discretized as

$$\begin{aligned}
\left(\varepsilon^{(h)}_{11,3}\right)^{I0} &= \sum_{J=1}^{n_I}\left[\frac{1}{h}\phi^{JI}\,\hat{\varepsilon}^J_{11(u)} - \frac{1}{h}\phi^{JI}\,\hat{\varepsilon}^J_{11(l)}\right],\\
\left(\varepsilon^{(h)}_{22,3}\right)^{I0} &= \sum_{J=1}^{n_I}\left[\frac{1}{h}\phi^{JI}\,\hat{\varepsilon}^J_{22(u)} - \frac{1}{h}\phi^{JI}\,\hat{\varepsilon}^J_{22(l)}\right],\\
\left(\varepsilon^{(h)}_{13,1}\right)^{I0} &= \frac{1}{2}\sum_{J=1}^{n_I}\left[\phi_{,1}^{JI}\,\hat{\varepsilon}^J_{13(u)} + \phi_{,1}^{JI}\,\hat{\varepsilon}^J_{13(l)}\right],\\
\left(\varepsilon^{(h)}_{23,2}\right)^{I0} &= \frac{1}{2}\sum_{J=1}^{n_I}\left[\phi_{,2}^{JI}\,\hat{\varepsilon}^J_{23(u)} + \phi_{,2}^{JI}\,\hat{\varepsilon}^J_{23(l)}\right].
\end{aligned} \tag{47}$$

Using Eq. (47) and neglecting the body forces, the nodal values $\hat{\tilde{\varepsilon}}^I_{33(u)}$ and $\hat{\tilde{\varepsilon}}^I_{33(l)}$ are expressed in terms of the nodal strains calculated directly from the displacements as follows

$$\hat{\tilde{\varepsilon}}^I_{33(u)} = \hat{\varepsilon}^I_{33(u)} + \frac{h}{2}\sum_{J=1}^{n_I}\boldsymbol{\Psi}^{JI}_{(0)}\,\hat{\boldsymbol{\varepsilon}}^J,\;\; \hat{\tilde{\varepsilon}}^I_{33(l)} = \hat{\varepsilon}^I_{33(l)} - \frac{h}{2}\sum_{J=1}^{n_I}\boldsymbol{\Psi}^{JI}_{(0)}\,\hat{\boldsymbol{\varepsilon}}^J,\;\; I=1,2,...,N, \tag{48}$$

where $\boldsymbol{\Psi}^{JI}_{(0)}$ is defined as

$$\begin{aligned}
\boldsymbol{\Psi}^{JI}_{(0)} = -\frac{1}{C_{3333}}\big[&\tfrac{1}{h}C_{3311}\phi^{JI} \quad \tfrac{1}{h}C_{3322}\phi^{JI} \quad 0 \quad 0 \quad \tfrac{1}{2}C_{2323}\phi_{,2}^{JI} \quad \tfrac{1}{2}C_{1313}\phi_{,1}^{JI} \quad \cdots\\
&\cdots \quad -\tfrac{1}{h}C_{3311}\phi^{JI} \quad -\tfrac{1}{h}C_{3322}\phi^{JI} \quad 0 \quad 0 \quad \tfrac{1}{2}C_{2323}\phi_{,2}^{JI} \quad \tfrac{1}{2}C_{1313}\phi_{,1}^{JI}\big].
\end{aligned} \tag{49}$$

If Eqs. (39) and (43) are employed in Eqs. (48), the nodal strains on the right-hand sides of relations (48) are computed in dependence of the nodal displacements as

$$\begin{aligned}
\hat{\tilde{\varepsilon}}^I_{33(u)} &= \sum_{J=1}^{n_I}\left(\mathbf{B}_3^T\right)^{JI}_{(0)}\hat{\mathbf{u}}^J + \frac{h}{2}\sum_{J=1}^{n_I}\left[\boldsymbol{\Psi}^{JI}_{(0)}\sum_{K=1}^{n_J}\mathbf{B}^{KJ}\hat{\mathbf{u}}^K\right],\\
\hat{\tilde{\varepsilon}}^I_{33(l)} &= \sum_{J=1}^{n_I}\left(\mathbf{B}_3^T\right)^{JI}_{(0)}\hat{\mathbf{u}}^J - \frac{h}{2}\sum_{J=1}^{n_I}\left[\boldsymbol{\Psi}^{JI}_{(0)}\sum_{K=1}^{n_J}\mathbf{B}^{KJ}\hat{\mathbf{u}}^K\right], \quad I=1,2,...,N.
\end{aligned} \tag{50}$$

Herein, $\left(\mathbf{B}_3^T\right)^{JI}_{(0)}$ stands for the third row of the 3D strain-displacement matrix calculated at the point $\mathbf{X}^I_{(0)}$ by means of Eq. (40), and the strain-displacement matrix in the second term on the right-hand side is defined as $\mathbf{B}^{KJ} = \left[\left(\mathbf{B}^{KJ}_{(u)}\right)^T \quad \left(\mathbf{B}^{KJ}_{(l)}\right)^T\right]^T$.

Finally, the nodal strain vector may be written in the following well-known discretized strain-displacement form as

$$\hat{\tilde{\boldsymbol{\varepsilon}}}^I = \sum_{M=1}^{\tilde{n}_I} \tilde{\mathbf{B}}^{MI}\,\hat{\mathbf{u}}^M,\ \ I = 1,2,...,N, \tag{51}$$

where $\tilde{\mathbf{B}}^{MI}, M = 1,2,...,\tilde{n}_I$, are the strain-displacement matrices calculated at $\mathbf{X}^I_{(0)}$ using Eq. (40), except for the terms associated with ε_{33}, which are derived from Eqs. (50). $\tilde{n}_I$ stands for the total number of the nodes influencing the nodal strain values $\hat{\tilde{\varepsilon}}^I_{33(u)}$ and $\hat{\tilde{\varepsilon}}^I_{33(l)}$.

After inserting (51) into the discretized LWF of equilibrium equations (34) and (35), the following system of equations with only the nodal displacements as unknowns is obtained for each local sub-domain

$$\sum_{J=1}^{N_I}\left[\int_{L_S^I}\mathbf{N}\mathbf{D}\boldsymbol{\Phi}^J_{\varepsilon}\mathrm{d}\Gamma+\int_{\Gamma^I_{Su}}\mathbf{N}\mathbf{D}\boldsymbol{\Phi}^J_{\varepsilon}\mathrm{d}\Gamma\right]\sum_{M=1}^{\tilde{n}_J}\tilde{\mathbf{B}}^{MJ}\,\hat{\mathbf{u}}^M-\alpha\sum_{J=1}^{n_I}\left(\int_{\Gamma^I_{su}}\boldsymbol{\Phi}^J_u\mathrm{d}\Gamma\right)\hat{\mathbf{u}}^J$$
$$=-\int_{L^I_{St}}\mathbf{t}\,\mathrm{d}\Gamma-\int_{\Omega^I_s}\mathbf{b}\,\mathrm{d}\Omega-\alpha\int_{\Gamma^I_{su}}\bar{\mathbf{u}}\,\mathrm{d}\Gamma, \tag{52}$$

$$\sum_{J=1}^{N_I}\left[\int_{L_S^I}X^3\mathbf{N}\mathbf{D}\boldsymbol{\Phi}^J_{\varepsilon}\,\mathrm{d}\Gamma+\int_{\Gamma^I_{Su}}X^3\mathbf{N}\mathbf{D}\boldsymbol{\Phi}^J_{\varepsilon}\mathrm{d}\Gamma-\int_{\Omega^I_s}\nabla\mathbf{v}_1^T\,\mathbf{D}\boldsymbol{\Phi}^J_{\varepsilon}\mathrm{d}\Omega\right]\sum_{M=1}^{\tilde{n}_J}\tilde{\mathbf{B}}^{MJ}\,\hat{\mathbf{u}}^M$$
$$-\alpha\sum_{J=1}^{n_I}\left(\int_{\Gamma^I_{su}}X^3\,\boldsymbol{\Phi}^J_u\,\mathrm{d}\Gamma\right)\hat{\mathbf{u}}^J=-\int_{L^I_{St}}X^3\,\mathbf{t}\,\mathrm{d}\Gamma-\int_{\Omega^I_s}X^3\,\mathbf{b}\,\mathrm{d}\Omega-\alpha\int_{\Gamma^I_{su}}X^3\,\bar{\mathbf{u}}\,\mathrm{d}\Gamma,$$
$$I=1,2,...,N. \tag{53}$$

In the plate analysis, the body forces may usually by neglected in engineering computations, and therefore the domain integrals on the right-hand sides may be omitted. Using a node-by-node numerical assemblage procedure, the global equations on the structural level are derived.

5 Numerical examples

In the following, deformation responses of rectangular plates with various boundary conditions are considered as numerical examples. The plates are discretized by

uniform grids, and LWFs are calculated over the cylindrical local sub-domains. The essential boundary conditions are imposed by applying the penalty method, where the penalty parameter is set to $\alpha = 10^9$.

The MLS functions with the first, second and fourth order complete polynomial basis, labeled as MLS1, MLS2 and MLS4, are used. For all MLS functions the 4^{th} order spline weighting functions are employed. In all examples, both the test domain radius R_{tr} and the support domain radius R_t are normalized by the nodal distance d defined in Fig. 3. Thereby, the test domain is defined as the supporting domain of the test function and the support domain denotes the supporting domain of the nodal MLS shape function.

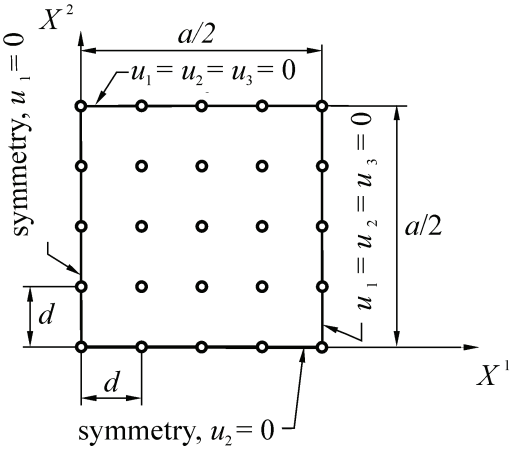

Figure 3: Discretization and the essential boundary conditions for the clamped plate

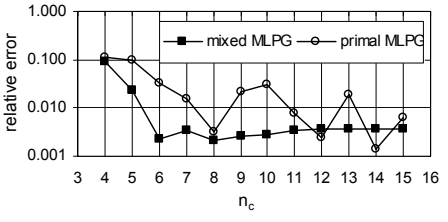

Figure 4: The influence of the circular number of Gaussian points n_c on the solution accuracy for $n_r = 2$ (81 nodes)

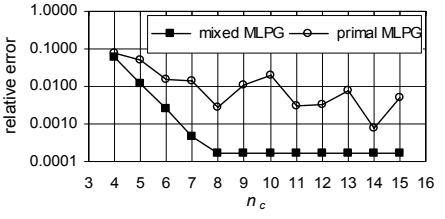

Figure 5: The influence of the circular number of Gaussian points n_c on the solution accuracy for $n_r = 2$ (289 nodes)

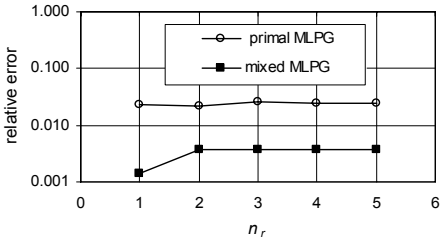

Figure 6: The influence of the radial number of Gaussian points n_r on the solution accuracy for $n_c = 9$ (81 nodes)

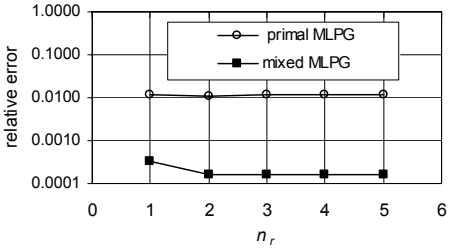

Figure 7: The influence of the radial number of Gaussian points n_r on the solution accuracy for $n_c = 9$ (289 nodes)

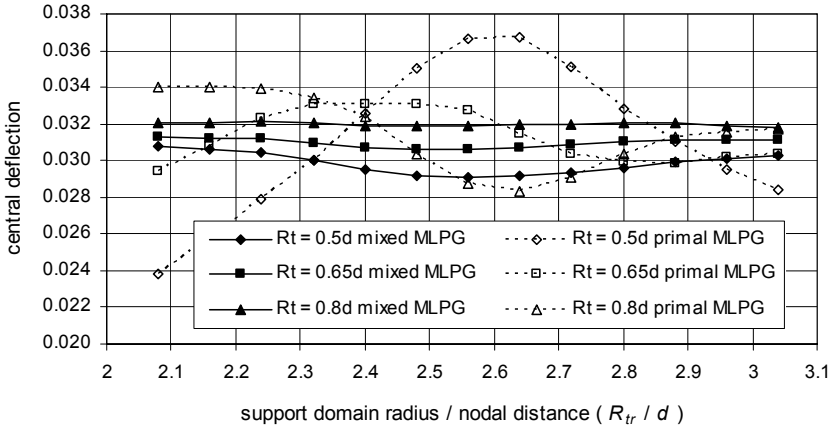

Figure 8: The influence of the test and support domain sizes on the solution accuracy for 81 nodes (clamped thick plate with $\nu = 0.0$)

The meshless results are compared with the finite elements solutions obtained by using the Msc.NASTRAN program package. The hexahedral finite elements are employed, in which the reduced integration is applied for the alleviation of shear locking.

5.1 Clamped thick square plate

In order to better expose some inherent numerical features of the proposed mixed approach, such as the efficiency of numerical integration or the absence of the Poisson's thickness locking effect, deformation responses of a clamped square plate are investigated in the first numerical example. In addition, the aim of the following numerical experiments is to demonstrate the numerical superiority of the presented

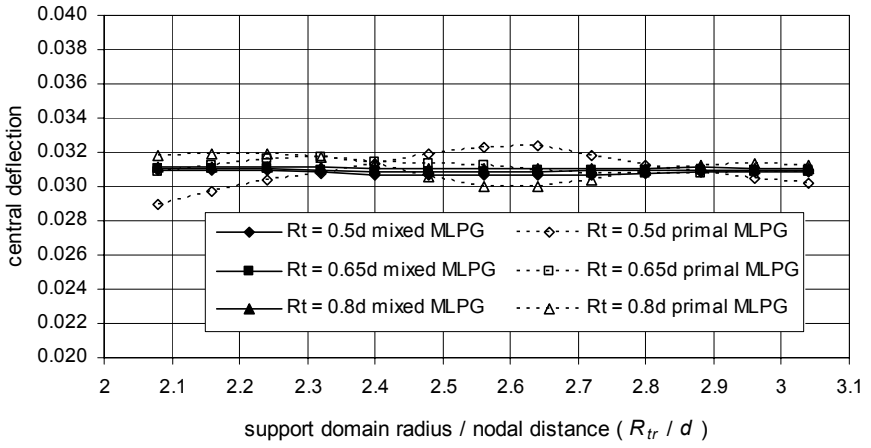

Figure 9: The influence of the test and support domain sizes on the solution accuracy for 289 nodes (clamped thick plate with $\nu = 0.0$)

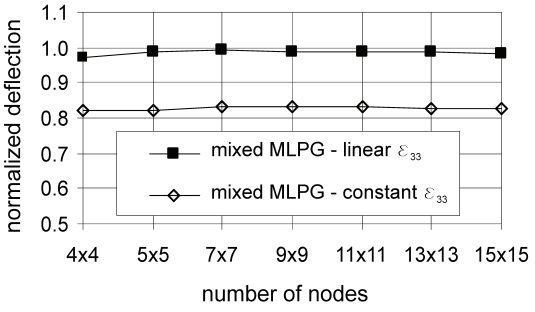

Figure 10: Convergence of the plate central deflection for the linear and constant distribution of ε_{33} through the thickness (clamped thick plate with $\nu = 0.3$)

mixed formulation over the primal MLPG method. Since it is well known that the primal MLPG formulations are prone to locking in the thin plate limit, a thick plate is analyzed so as to circumvent the difficulties associated with the shear locking phenomena. Information on the applied primal MLPG formulation may be found in [Sorić, Li, Jarak and Atluri (2004)] and the references therein.

The plate is clamped along the outer edges, and it is subjected to the uniformly distributed load $q = 200$ acting over the upper surface. The plate span to thickness ratio is set to $a/h = 10$ with the thickness being $h = 1$. The Young's modulus of the material is $E = 10.92 \cdot 10^5$. Due to symmetry, only one quarter of the plate is discretized by uniform grids. Fig. 3 shows the applied essential boundary conditions

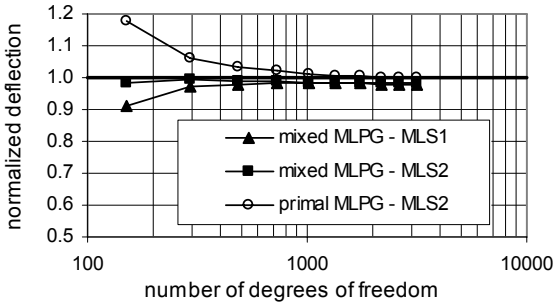

Figure 11: Convergence study in comparison with the primal MLPG formulation (clamped plate thick with $\nu = 0.3$)

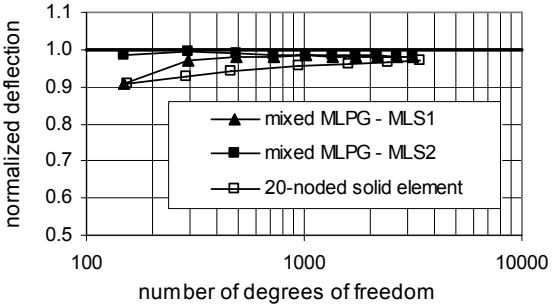

Figure 12: Convergence study in comparison with the solid finite elements (clamped thick plate with $\nu = 0.3$)

and the grid consisting of 5×5 node couples.

5.1.1 Numerical integration of the LWF

It is well known that numerical integration is one of the problematic issues in the meshless methods. Therefore, the performance of the proposed mixed approach considering the numerical cubature of the LWF is inspected first. In order to concentrate only on the integration of the weak forms itself, the Poisson's ratio of the material is set to zero, $\nu = 0$, avoiding the appearance of the Poisson's locking effect. Accordingly, the procedure for the elimination of the Poisson's thickness locking effect described in section 4 is not used in the mixed formulation. In the primal MLPG formulation LWF (6) and (7) is discretized by approximating only the displacement field, where the linear distribution over the thickness is assumed.

The plate is discretized by 81 (9x9) and 289 (17x17) node couples. All calculations are performed by using MLS2, while the test and the support domain radii are set to $R_t = 0,7\,d$ and $R_{tr} = 2,2\,d$, respectively.

The accuracy of the solution for the plate central deflection is checked for different numbers of integration points. In both the mixed and primal formulations the simple Gaussian numerical integration scheme is employed, where 2 integration points are used over the thickness. The numbers of points in the circular and radial direction of the local sub-domain are varied, and are labeled as n_c and n_r, respectively. The results of the tests are shown in Figs. 4 to 7. The relative error is defined as $(w - w_r)/w_r$, where w is a meshless solution obtained for some particular choice of n_c and n_r, and w_r is a referent value calculated by using the sufficiently large values for n_c and n_r, $n_c = n_r = 20$.

It is obvious from Figs. 4 and 5 that in the primal MLPG method the number of the quadrature points in the circular direction affects the stability of the solution more severely than in the proposed mixed algorithm. In the primal MLPG method, the oscillation of the solution values is clearly visible, and the solution accuracy is not significantly improved even if the finer nodal grid is used. On the other hand, in the mixed approach $n_c = 7$ provides acceptable solution accuracy and the results are stabilized if more points are used. From Figs. 6 and 7 it can be observed that for both approaches the solution values don't depend significantly on the number of quadrature points in the radial direction and that 2 points are sufficient for obtaining stable results. However, higher accuracy is obtained if the mixed approach is applied.

5.1.2 Effects of the sizes of test and support domains on the solution accuracy

The sizes of the test and the support domains may significantly affect the solution accuracy in the MLPG method. Hence, the influences of these parameters on the solution for the plate central deflection has been investigated, and the results are plotted in Figs. 8 and 9. Again, discretization is performed by using 9x9 and 17x17 node couples. All results are obtained by applying 9 quadrature points in the circular direction, $n_c = 9$, and 2 points in the radial direction, $n_r = 2$, in each local sub-domain. Furthermore, the Poisson's ratio is set to zero, $\nu = 0$, and therefore no procedures for the elimination of the Poisson's thickness locking effect are employed.

Evidently, in the mixed approach the influence of the support domain size on the solution values is not as pronounced as in the primal MLPG formulation and it becomes almost negligible if the finer nodal grid is used. Therefore, the values that are close to the minimum necessary support domain size may be chosen for numerical calculations so as to increase the numerical efficiency. However, the size

of the test domain influences the solution accuracy significantly, although not as much as in the primal MLPG method. Nevertheless, this effect again diminishes remarkably if more nodes are applied for discretization.

5.1.3 The Poisson's thickness locking effect

In order to demonstrate the efficiency of the procedure for the elimination of the Poisson's thickness locking effect, the Poisson's ratio is set to $\nu = 0.3$. In the primal formulation the hierarchical quadratic interpolation over the thickness is assumed for u_3 to avoid the Poisson's thickness locking [Sorić, Li, Jarak and Atluri (2004)]. All calculations are performed by using 2 quadrature points in the radial direction, $n_r = 2$. For the mixed approach 7 Gaussian points are employed in the circular direction, $n_c = 7$, while for the primal MLPG formulation $n_c = 11$.

The efficiency of the proposed procedure for the elimination of the thickness locking effect is displayed in Fig. 10, where the convergence rate is compared with the result obtained by using the algorithm in which the nodal strains are calculated by means of the unmodified strain-displacement relations (39). The values for the central plate deflection are normalized by the analytical solution [Srinivas and Rao (1973)]. Obviously, the convergence to the referent analytical solution is achieved if the proposed approach with the linear distribution over the thickness for ε_{33} is employed, indicating that the Poisson's thickness locking phenomenon is efficiently eliminated.

In addition, the convergence rates of the mixed meshless formulation are compared with the results obtained by means of the primal MLPG formulation [Sorić, Li, Jarak and Atluri (2004)], as well as the brick-type solid finite elements from NASTRAN, and the results are presented in Figs. 11 and 12.

In the mixed formulation both the MLS1 and MLS2 functions have been used. In both cases the test domain radius is $R_t = 0.65\,d$, while the support domain radius has been set to $R_{tr} = 1.25\,d$ for MLS1 and $R_{tr} = 2.15\,d$ for MLS2. On the other hand, in the primal MLPG method only MLS2 with $R_t = 0.8\,d$ and $R_{tr} = 2.4\,d$ is applied. It is to note that no convergence could be achieved in the primal method if MLS1 is applied.

As may be seen, the mixed formulation demonstrates better convergence rates than the primal method even if MLS1 is used. Moreover, Fig. 12 portrays that the convergence rates are also higher than that obtained by using the NASTRAN hexahedral finite elements.

5.2 Clamped thin square plate

As the next example, a clamped thin square plate with the thickness $h = 1$ and the side length $a = 100$ is subjected to the uniformly distributed load $q = 0.1$ over the upper surface. The material data are the Poisson's ratio $\nu = 0.3$ and the Young's modulus $E = 10.92 \cdot 10^5$. Again, only one quadrant of the plate is discretized by uniform grids.

The influence of the test and support domain sizes on the solution accuracy is displayed in Figs. 13 and 14 for the mixed formulation if MLS1 and MLS2 are employed. Discretization is performed by using 289 (17x17) node couples. All results are normalized by using the analytic solution [Timoshenko and Voinowsky-Krieger (1985)]. As evident, the considerable oscillations around the analytic value are exhibited, especially for the higher values of the support domain radius R_{tr}. However, for both MLS functions stabilization is achieved for $R_t = 0.65d$. Hence, in order to increase numerical efficiency, the support domain radii $R_{tr} = 1.25\,d$ for MLS1 and $R_{tr} = 2.15\,d$ for MLS2, which are close to the minimum necessary values for R_{tr}, are used in combination with $R_t = 0.65d$ in the subsequent numerical tests.

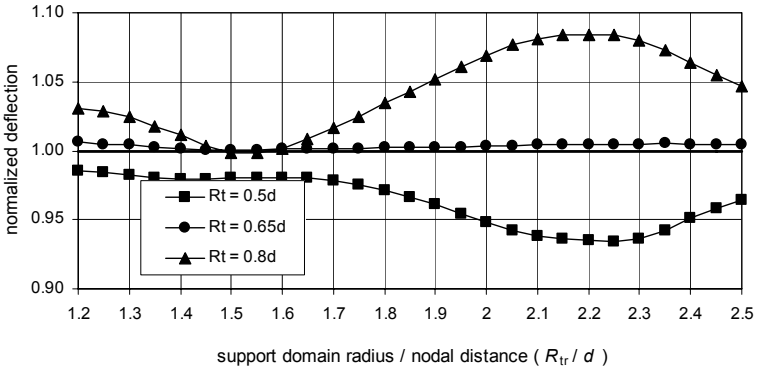

Figure 13: The influence of the test and support domain sizes on the solution accuracy for MLS1 (clamped thin plate)

In addition, the convergence rates for the plate central deflections computed by the proposed mixed approach are compared with the solid hexagonal finite elements and the primal MLPG formulation solutions in Figs. 15 and 16. MLS1 and MLS2 are used in the mixed approach, while MLS4 is applied in the primal formulation.

As may be observed in Fig. 15, the mixed formulation demonstrates better accuracy and higher convergence rates in comparison to the finite element solutions, indicat-

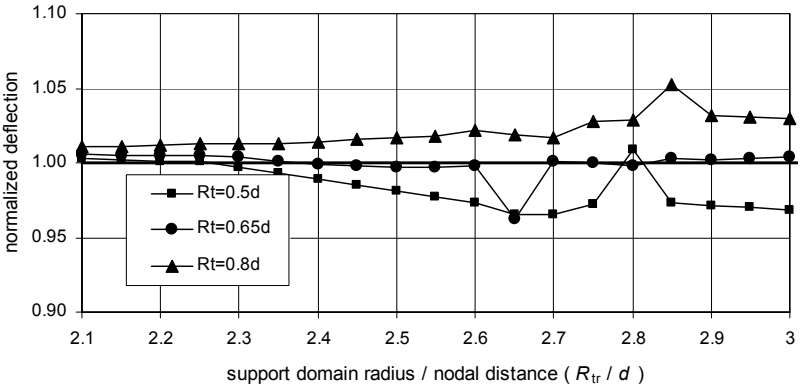

Figure 14: The influence of the test and support domain sizes on the solution accuracy for MLS2 (clamped thin plate)

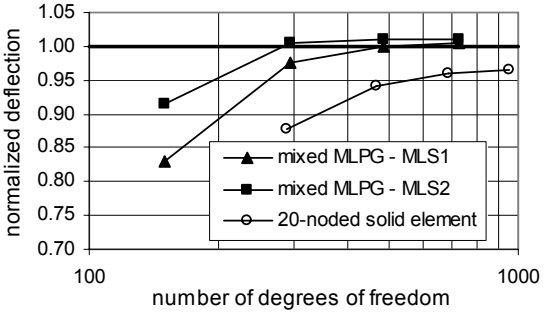

Figure 15: Convergence study in comparison with the solid finite elements (clamped thin plate)

ing that the undesirable shear locking effect is efficiently overcome. Fig. 16 shows that the convergence rate is higher than that of the primal MLPG formulation even though the low-order MLS functions are used. Moreover, it should also be noted that the lower order of the MLS functions increases the numerical efficiency of the mixed formulation by allowing the use of the smaller sizes of the support domains, as well as fewer quadrature points.

The sensitivity of the proposed mixed approach on the shear locking effect has further been tested by increasing the plate span to thickness ratio, as shown in Fig. 17. As evident, shear locking is completely eliminated even for the very thin plates if MLS2 is used.

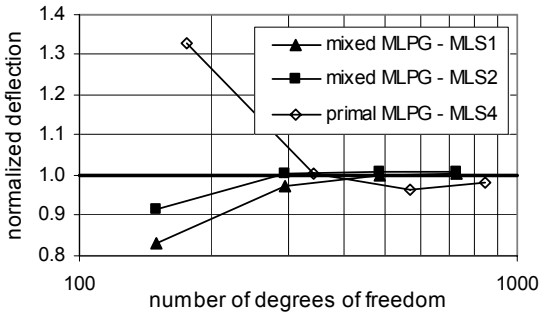

Figure 16: Convergence study in comparison with the primal MLPG formulation (clamped thin plate)

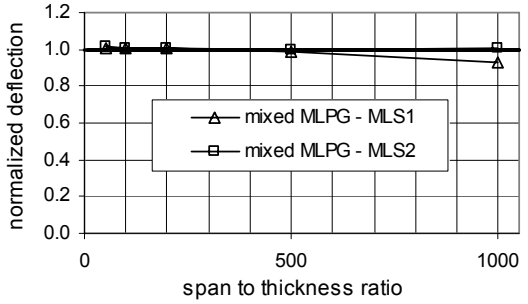

Figure 17: Central deflection vs. plate span to thickness ratio (clamped thin plate)

5.3 Simply supported thin square plate

Finally, a thin simply supported plate under uniformly distributed load is analyzed. The geometry, load value and material properties are the same as in the previous example. Again, symmetry conditions are applied and only one quadrant of the plate is discretized by uniform grids. The applied essential boundary conditions and the discretization grid consisting of 5x5 node couples are shown in Fig. 18.

The results of the convergence tests are presented in Figs. 19 and 20, where the central deflection is again normalized by using the analytic solution [Timoshenko and Voinowsky-Krieger (1985)]. The computations have been performed by using the same values of the test and support domain radii as in the example considering the thin clamped plate. MLS1 and MLS2 are used in the mixed algorithm, while MLS4 is again applied in the primal MLPG formulation.

From Fig. 19 it can be concluded that for this problem the convergence rates are

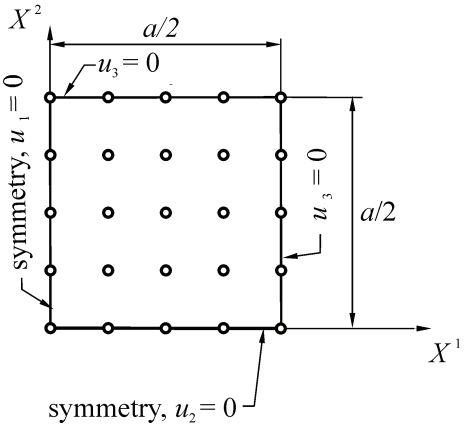

Figure 18: Discretization and the essential boundary conditions for the simply supported plate

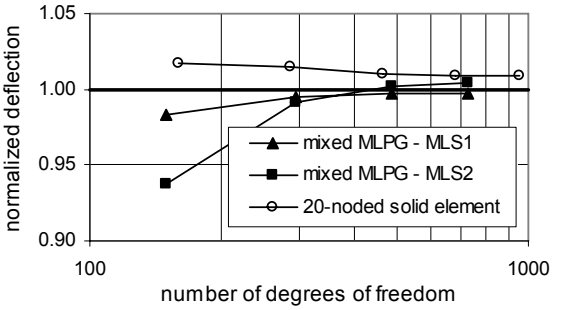

Figure 19: Convergence study in comparison with the solid finite elements (simply supported thin plate)

comparable to those obtained by FEM. However, it is evident that the proposed formulation achieves high accuracy even if coarse discretization grids are applied. Fig. 20 shows that the mixed formulation is again superior to the primal MLPG method, as expected. The sensitivity of the proposed mixed approach on the shear locking effect has again been tested by increasing the plate span to thickness ratio. The results in Fig. 21 display that shear locking is completely eliminated for this problem even if MLS1 is used.

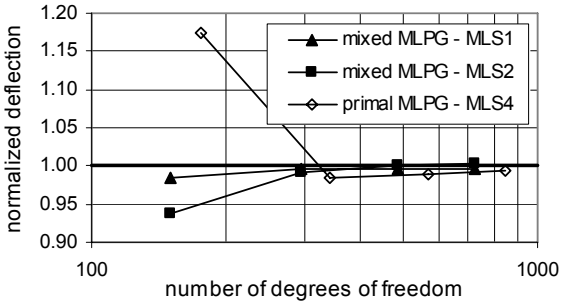

Figure 20: Convergence study in comparison with the primal MLPG formulation (simply supported thin plate)

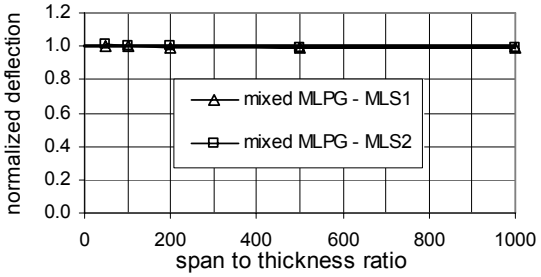

Figure 21: Central deflection vs. plate span to thickness ratio (simply supported thin plate)

6 Conclusion

A new mixed MLPG formulation based on the interpolation of both strains and displacements has been proposed for the analysis of plate structures. The kinematics of a 3-D solid is applied, allowing the use of complete 3-D constitutive equations. Discretization is performed only by the nodes located on the upper and lower structure surfaces. The governing equations are derived by approximating the strains directly as independent variables in the local weak forms of the equilibrium equations. The nodal strains are then eliminated from the equations by enforcing the standard strain-displacement relations only at the nodes, and the closed system of equations with only the nodal displacements as unknown variables is obtained. The approximation of all field variables is performed by employing the same MLS functions in the in-plane directions, while linear polynomials are used in the thickness direction. The shear locking phenomenon in the thin plate limit is successfully sup-

pressed and a new efficient procedure for the elimination of the Poisson's thickness locking effect is developed.

The proposed formulation is numerically more efficient that the primal MLPG method, where only displacements are approximated. The mixed approach decreases the continuity requirements for the trial functions and allows the use of the lower–order MLS functions than in the primal method, even in the thin plate limit. Therefore, the smaller support and test domains may be used and fewer Gaussian points are needed for numerical integration than in the primal MLPG formulations. Moreover, the differentiation of the MLS functions at each quadrature point in the local sub-domains is avoided. Consequently, the influence of the support and test domain sizes on solution accuracy is not as pronounced as in the primal MLPG method and numerical costs are further reduced. As demonstrated by the presented numerical examples, the new formulation possesses very good convergence rate and solution accuracy.

References

Atluri S.N.; Han Z.D.; Rajendran M.J. (2004): A New Implementation of the Meshless Finite Volume Method, Through the MLPG "Mixed" Approach, *CMES: Computer Modeling in Engineering & Sciences*, vol. 6, pp. 491–513

Atluri, S.N. (2004): The Meshless Method (MLPG) for Domain & BIE Discretization, Tech Science Press, Forsyth, USA.

Atluri, S.N.; Shen, S. (2005): Simulation of a 4th Order ODE: Illustration of Various Primal & Mixed MLPG Methods, *CMES: Computer Modeling in Engineering & Sciences*, vol. 7, pp. 241-268.

Atluri, S.N.; Zhu, T. (1998): A new Meshless Local Petrov-Galerkin (MLPG) approach in computational mechanics, *Computational Mechanics*, vol. 22, pp. 117-127.

Atluri, S.N.; Zhu, T.-L. (2000): The Meshless Local Petrov-Galerkin (MLPG) approach for solving problems in elasto-statics, *Computational Mechanics*, vol. 25, pp. 169-179.

Chen, J-S.; Wang, D. (2006): A constrained reproducing kernel particle formulation for shear deformable shell in Cartesian coordinates, *Int. J. Numer. Mech. Engng.*, vol. 68, pp. 151-172.

Donning, B.M.; Liu, W.K. (1998): Meshless methods for shear-deformable beams and plates, *Computer Methods in Applied Mechanics and Engineering*, vol. 152, pp. 47-71.

Fasshauer, G.E. (2007): *Meshfree Approximation Methods with MATLAB*, World

Scientific Publishing, Singapore, Singapore.

Ferreira, A.J.M; Roque, C.M.C; Jorge R.M.N. (2006): Modelling cross-ply laminated elastic shells by a higher-order theory and multiquadrics, *Computers and Structures*, vol. 84, pp. 1288–1299.

Garcia, O.; Fancello, E.A.; de Barcellos C.S.; Duarte, C.A. (2000): hp-clouds in Mindlin's thick plate model. *International Journal for Numerical Methods in Engineering*, vol. 47, pp. 1381–1400.

Gilhooley, D.F.; Batra, R.C.; Xiao, J.R.; McCarthy, M.A.; Gillespie Jr., J.W. (2007): Analysis of thick functionally graded plates by using higher-order shear and normal deformable plate theory and MLPG method with radial basis functions, *Composite Structures*, vol. 80, pp. 539–552.

Han, Z.D; Rajendran, A.M.; Atluri, S.N. (2005): Meshless Local Petrov-Galerkin (MLPG) Approaches for Solving Nonlinear Problems with Large Deformations and Rotations. *CMES: Computer Modeling in Engineering & Sciences*, vol.10, no.1, pp.1-12.

Hauptmann, R.; Schweizerhof, K. (1998): A systematic development of solid-shell element formulations for linear and non-linear analyses employing only displacement degrees of freedom, *Int. J. Numer. Meth. Engng.*, vol. 42, pp. 49-69.

Jarak, T.; J. Sorić, J.; Hoster, J. (2007): Analysis of shell deformation responses by the Meshless Local Petrov-Galerkin (MLPG) approach. *CMES: Computer Modeling in Engineering & Sciences*, vol. 18, pp. 235-246.

Kanok-Nukulchai, W,; Barry, W.; Saran-Yasoontorn, K.; Bouillard, P.H. (2001): On elimination of shear locking in the element-free Galerkin method, *Int. J. Numer. Meth. Eng.*, vol. 52, pp. 705–725.

Klinkel, S.; Gruttmann, F.; Wagner, W. (2006): A robust non-linear solid shell element based on a mixed variational formulation, *Comput. Methods Appl. Mech. Engrg.*, vol. 195, pp. 179-201.

Krysl, P.; Belytschko, T. (1995): Analysis of thin plates by the element-free Galerkin method, *Computational Mechanics*, vol. 17, pp. 26-35.

Krysl, P.; Belytschko T. (1996): Analysis of thin shells by element-free Galerkin method, *Int. J. Solids Structures*, vol. 33, pp. 3057-3080.

Li, Q.; Sorić, J.; Jarak, T.; Atluri, S.N. (2005): A locking-free meshless local Petrov-Galerkin formulation for thick and thin plates, *Journal of Computational Physics*, vol. 208, pp. 116-133.

Li, S.; Hao, W.; Liu, W.K. (2000): Numerical simulations of large deformation of thin shell structures using meshfree method, *Computational Mechanics*, vol. 25, pp. 102–116.

Liu, G.R. (2003): *Mesh Free Methods: Moving beyond the Finite Element Method*, CRC Press, Boca Raton, USA.

Liu, L; Chua, L.P. ; Ghista, D.N. (2006): Element-free Galerkin method for static and dynamic analysis of spatial shell structures. *Journal of Sound and Vibration*, vol. 295, pp. 388–406.

Long, S.; Atluri, S.N. (2002): A Meshless Local Petrov-Galerkin Method for Solving the Bending Problem of a Thin Plate, *CMES: Computer Modeling in Engineering & Sciences*, vol. 3, pp. 53-63.

Noguchi, H.; Kawashima, T., Miyamura, T. (2000): Element free analyses of shell and spatial structures, *Int. J. Numer. Math. Engng.*, vol. 47, pp. 1215-1240.

Qian, L.F.; Batra, R.C.; Chen L.M. (2003): Elastostatic Deformations of a Thick Plate by using a Higher-Order Shear and Normal Deformable Plate Theory and two Meshless Local Petrov-Galerkin (MLPG) Methods, *CMES: Computer Modeling in Engineering & Sciences*, vol. 4, pp. 161-175.

Qian, L.F.; Batra, R.C.; Chen L.M. (2004): Static and dynamic deformations of thick functionally graded elastic plates by using higher-order shear and normal deformable plate theory and meshless local Petrov-Galerkin method, *Composites: Part B*, vol. 35, pp. 685–697.

Sladek, J.; Sladek, V.; Krivacek, J.; Aliabadi, M.H. (2007): Local boundary integral equations for orthotropic shallow shells, *International Journal of Solids and Structures*, vol. 44, pp. 2285–2303.

Sladek, J.; Sladek, V.; Mang, H.A. (2002): Meshless formulations for simply supported and clamped plate problems. *Int. J. Num. Meth. Engn*., vol. 55, pp. 359-375.

Sladek, J.; Sladek, V.; Mang, H.A. (2003): Meshless LBIE formulations for simply supported and clamped plates under dynamic load. *Computers and Structures*, vol. 81, pp. 1643-1651.

Sladek, J.; Sladek, V.; Wen, P.H.; Aliabadi, M.H. (2006): Meshless Local Petrov-Galerkin (MLPG) Method for Shear Deformable Shells Analysis, *CMES: Computer Modeling in Engineering & Sciences*, vol. 6, no. 2, pp. 103-117

Sorić, J.; Li, Q.; Jarak, T.; Atluri, S.N. (2004): Meshless Local Petrov-Galerkin (MLPG) formulation for analysis of thick plates, *CMES: Computer Modeling in Engineering & Sciences*, vol. 6, no. 4, pp. 349-357.

Srinivas, S.; Rao, A. K. (1973): Flexure of Thick Rectangular Plates, *J. Appl. Mech. ASME*, vol. 40, pp. 298-299.

Sze, K.Y. (2002): Three-dimensional continuum finite element models for plate/shell analysis. *Prog. Struct. Engng. Mater.*, vol. 4, pp. 400-407.

Tan, X.G.; Vu-Quoc, L. (2005): Optimal solid shell element for large deformable composite structures with piezoelectric layers and active vibration control, *Int. J. Numer. Mech. Engng.*, vol. 64, pp. 1981-2013.

Tan, X.G.; Vu-Quoc, L. (2005): Optimal solid shell element for large deformable composite structures with piezoelectric layers and active vibration control, *Int. J. Numer. Mech. Engng.*, vol. 64, pp. 1981-2013.

Tiago, C.; Leitão, V. (2007): Eliminating Shear-Locking in Meshless Methods: A Critical Overview and a New Framework for Structural Theories, in Advances in Meshfree Techniques, volume 5, *Computational Methods in Applied Sciences series*, Springer, pp. 123-145.

Timoshenko, S.; Voinowsky-Krieger, S. (1985): Theory of Plates and Shells, McGraw-Hill, London.

Wang, D.; Chen, J.-S. (2004): Locking-free stabilized conforming nodal integration for meshfree Mindlin-Reissner plate formulation. *Comput. Methods. Appl. Mech. Engrg.*, vol. 193, pp. 1065-1083.